Cytometry
PART A
Journal of the
International Society for
Advancement of Cytometry

A Quantitative Measure for Alterations in the Actin Cytoskeleton Investigated with Automated High-Throughput Microscopy

Julian Weichsel,[1] Nikolas Herold,[2] Maik J. Lehmann,[2] Hans-Georg Kräusslich,[2]
Ulrich S. Schwarz[1,3]*

[1]BioQuant, University of Heidelberg, Heidelberg, Germany

[2]Department of Infectious Diseases, Virology, University Hospital of Heidelberg, Heidelberg, Germany

[3]Institute for Theoretical Physics, University of Heidelberg, Heidelberg, Germany

*Correspondence to: Ulrich Schwarz, BioQuant 0013, University of Heidelberg, Im Neuenheimer Feld 267, Heidelberg, 69120, Germany

Email: ulrich.schwarz@bioquant.uni-heidelberg.de

ISAC
International Society for Advancement of Cytometry

● **Abstract**

The actin cytoskeleton modulates a large variety of physiological and disease-related processes in the cell. For example, actin has been shown to be a crucial host factor for successful infection by HIV-1, but the underlying mechanistic details are still unknown. Automated approaches open up the perspective to clarify such an issue by processing many samples in a high-throughput manner. To analyze the alterations in the actin cytoskeleton within an automated setting, large-scale image acquisition and analysis were established for JC-53 cells stained for actin. As a quantitative measure in such an automated approach, we suggest a parameter called image coherency. We successfully benchmarked our analysis by calculating coherency for both a biophysical model of the actin cytoskeleton and for cells whose actin architecture had been disturbed pharmacologically by latrunculin B or cytochalasin D. We then tested the influence of HIV-1 infection on actin coherency, but observed no significant differences between uninfected and infected cells.   © 2009 International Society for Advancement of Cytometry

● **Key terms**

actin cytoskeleton; biophysical modeling; image analysis; high-throughput microscopy; HIV-infection

SYSTEMS biology of animal cells tends to focus on biochemical aspects like gene expression and signal transduction. However, it is equally important to develop methods to study the structural and mechanical aspects of a cell. In particular, a complete understanding of the cell as an integrated system has to include models for the microtubule and actin cytoskeletons, as they determine mechanical stability (1) and spatially organize cellular processes such as signal transduction (2) and motor-based transport (3).

Because of its importance for the spatial coordination of the host cell, the cytoskeleton is also one of the major targets for changes induced by cellular pathogens (4,5). Despite the large medical relevance of this interaction, the exact underlying mechanisms are in many cases still unknown. In our study, we investigated HIV-1 as a medically highly relevant pathogen whose specific effect on the actin cytoskeleton is not yet well understood (6). Viruses rely on cellular metabolism for their replication and can be used also as probes to study the host system. Thus, viruses are also important tools to better understand the biology of the cell. In the case of HIV-1, binding to the cell via its envelope glycoprotein has been reported to induce actin remodeling (7), calcium signaling (8), and chemotaxis (7). The life cycle of HIV-1 is known to relate to various additional aspects of the cytoskeleton. This includes virus surfing along actin rich cell protrusions to reach the cell body (9), crossing the cell cortex after fusion (10), transport towards the nucleus (11), and spreading of the newly synthesized virions to new target cells in the proximity (12,13). Indeed, it has been shown earlier that an intact actin cytoskeleton is necessary for successful HIV-1

infection (14), but the details of this phenomenon are still unknown. The rapidly increasing availability of high-throughput microscopy setups now opens up the perspective that such an issue can be clarified within an automated approach. However, such an approach requires the development of new techniques for cell culture and data processing, including quantitative measures which are able to characterize alterations in the host cytoskeleton in a high-throughput manner.

Recently, large efforts have been made to find meaningful measures describing the structural organization of cytoskeleton constituents on different length scales. On a subcellular scale, certain filament features like fiber length or orientation have been extracted from fluorescence microscopy images for actin bundles and microtubules (15), and from electron microscopy images for single actin fibers (16). In the latter case, the experimental data have been compared with theoretical models for actin networks (17). On a cellular level, cell-based screens have been developed to classify morphological phenotypes (18,19). This method has already been applied successfully to drug profiling (20), quantifying viral infection (21), and determining drug effects on cell adhesion (22).

Automated high-throughput imaging of infected cells combined with quantitative analysis of the actin cytoskeleton opens the perspective to establish the precise role of the actin cytoskeleton upon HIV-1-entry. In general, this approach combines several advantages. First, automation permits analysis of very large data sets, including independent repetitions to account for morphological variability in a biological system. Second, the structural phenotype may be subtle, and thus, not accessible to the human eye. As an established cell culture system for infection, we used a HeLa-derived reporter cell line in a setup suitable for automated high-throughput microscopy. To analyze a large amount of images in an automated fashion, appropriate methods have to be developed to quantify morphological changes in the actin cytoskeleton. Here, we combined automated fluorescence microscopy and image processing with biophysical modeling to arrive at a validated workflow which allows us to quantify structural changes in the actin cytoskeleton of adherent cells.

A fluorescence image of a biological system is a two-dimensional quantized representation of the density of a specific marker molecule, and care has to be taken to extract a relevant and operative measure from these images. Here, we suggest that image coherency is an adequate quantitative parameter for the problem at hand. In contrast to pattern recognition approaches like neural networks or vector-support machines based on motion-invariant image features like the Haralick texture features or Zernike moments (23–25), which are well-suited for classification of distinct subcellular phenotypes, the coherency measure appears to be particularly suited to characterize gradual changes in fibrous textures like the actin cytoskeleton. By its definition, coherency extracts the relative strength of the edges of structures compared to their surroundings (26). Thus, the parameter is a measure for the quality and amount of clear structures in an image. It has been used before to detect features of moving filaments in actin-myosin motility assays (27), but not yet as a measure for the

organization of the actin cytoskeleton. To benchmark its value for characterizing the actin cytoskeleton, we followed a dual strategy. On the theory side, we used a simple model for the random geometry of the actin cytoskeleton, the random fiber or Mikado model, which consists of a random arrangement of cross-linked filaments (28), and applied our image processing procedure to a large number of its realizations. On the experimental side, we perturbed the actin cytoskeleton by using depolymerizing actin drugs (latrunculin B and cytochalasin D). Having successfully established these controls, we then assessed the impact of HIV-1 on actin coherency. We did not observe significant differences in actin coherency between uninfected and virus-infected cells. This could either mean that HIV's influence on the actin cytoskeleton is not related to detectable structural alterations, or that structural changes are of a more subtle nature than monitored in our setup. In future, our setup can be applied to other combinations of viruses and cell types.

MATERIALS AND METHODS

Cell Culture and HIV-Infection

Since its discovery as causative agent of AIDS in 1983 (29), extensive efforts have been made to study HIV-1. Cell lines are a reliable system to reproducibly analyze viral replication. Besides lymphocyte-derived suspension cell lines, HIV-1 can also infect adherent HeLa-derived cell lines like JC-53 (30). These cell lines were engineered to express the HIV-1 receptor CD4 (31) and its co-receptors CXCR4 and/or CCR5 and are thus fully permissive for HIV-1 infection.

JC-53 cells adhere to surfaces suitable for two-dimensional tissue culture. As they are flat, they occupy a large area on the cover glass which is virtually in one plane. Staining of actin with fluorescent phalloidin conjugates exhibits actin structures such as focal adhesions, stress fibers, filopodia, and the actin cortex, which can be easily monitored by epi-fluorescence microscopy. Furthermore, the large amount of actin structures in the focal plane on the cover glass combines several advantages: (a) The signal-to-noise ratio is excellent. (b) The choice of the very bottom of the cell decreases blurring from out-of-focus signal to a minimum as there is no blurring from below and only a small proportion from the less actin-dense structures from above. (c) The point-spread-function is sharpest close to the cover glass (32).

For treatment of JC-53 with cytochalasin D and latrunculin B, cells were cultured in Dulbecco's modified Eagle medium (DMEM)-Glutamax (Gibco) with 10% fetal calf serum (Biochrom) and penicillin/streptomycin at 37°C and 5% CO_2. Before seeding, cells were washed and detached using 3 mM EDTA in PBS. A total of 3×10^4 cells was seeded into a well of a 8-chambered Lab-Tek cover glass (Nunc), coated with bovine fibronectin (Sigma Aldrich), and allowed to settle down for 3 h. Subsequently, they were incubated for another 40 min with cytochalasin D or latrunculin B (Biomol) prior to fixation and permeabilization according to the PHEMO fixation protocol (33). Cells were blocked for 30 min with 1% BSA in PBS and stained for actin and microtubules using a

monoclonal mouse-anti-α-tubulin antibody (Cell Signal), a rabbit-anti-mouse IgG coupled to Atto-633 secondary antibody (Sigma Aldrich), and phalloidin-TRITC (Invitrogen) at a concentration of 1 μg/ml.

For the preparation of non-infectious fluorescent HIV-1 either bearing or lacking the viral envelope glycoprotein, HEK 293T cells were transfected using the PEI (polyethylene imine, Sigma Aldrich) method with plasmids encoding for (a) an Env-deficient NL4-3-derived non-infectious HIV-1 wt, (b) an MA-eGFP-tagged variant of (a), and (c) with or without NL4-3-derived Env-plasmid at a ratio of 3:3:1 (34). Supernatants were harvested after 48 h and purified through a 20% sucrose cushion. Fibronectin-coated 8-chambered Lab-Teks were pre-coated with fluorescent HIV-1, bearing or lacking the Env gly-coprotein, for 1 h at 4°C. JC-53 cells were added and allowed to settle down. Pre-coating with virus thus allowed us to preferentially explore the Env-specific effect of HIV-1 on the actin cytoskeleton in the defined focus plane.

Automated Microscopy and Image Processing

For this study, we used an Olympus inverted autofocus multicolour epi-fluorescence microscope with an automated stage and a 60x oil immersion objective (NA = 1.35). The oil immersion objective was used to obtain high resolution images. To combine it with the high throughput approach requiring large movements of the objective, oil was applied to the entire cover glass (alternatively an oil pump could be used to continuously deliver oil to the objective). Images were recorded by a 12bit EM-CCD camera. Acquisition of three-colour z-stacks at 100 positions for each well of a Lab-Tek 8-chambered cover glass was carried out sequentially without any interruption to ensure a maximum of comparability. The positions were defined as a 10×10 matrix with an arbitrary row and column spacing of 300 μm, whereas the center point of the matrix was determined manually to be in the middle of the chamber. Z-stacks ($n = 20$; $\Delta s = 400$ nm) were acquired to compensate for failure of autofocus and to be able to analyze the whole cell actin morphology or virus distribution, if necessary. Using these methods, we performed a screening-like image acquisition resulting in 48,000 raw images for a single experimental setup to be computationally processed and analyzed.

The complete image processing was done in Matlab. Because for our purposes the 12bit image depth was not required, each image was first converted into an 8bit grays-cale version to decrease computational effort. Then, the mean local contrast of all associated actin stained images was approximated for each z-stack. For this purpose, the cell area lying whithin the stack was estimated by applying Matlab's graythresh function which uses Otsu's method (35) for segmentation to one represent image of the stack. After subsequent hole filling of the cell area, the relative local contrast, i.e., the mean relative difference of a center pixel to all of its eight neighbors, was calculated for a large number of random positions within the boundaries of the cell. Afterwards, the mean of the contrasts from all of these positions was taken as an estimate for the mean local contrast

of the image. For each z-stack, the image with the highest mean local contrast was chosen for the following evaluation, assuming that it carries the most important structural features of the cytoskeleton. As the stacks were taken at random positions within the sample, not every image contained a sufficient amount of information to be evaluated. To cancel out empty or nearly empty image-stacks, the coherency (cf. the section "Coherency as a quantitative measure for structure") was calculated, and only those pictures exceeding a constant threshold for the total area of non-vanishing coherency pixel underwent further analysis. Feature analysis was performed, consisting of the calculation of the relative actin density per cell area, the relative coherency per cell area, the mean coherency per image, and the statistical evaluation of these parameters. We evaluated an estimator for the parameter-mean and its corresponding standard deviation from all images for each sample. This estimator was visualized in a box plot, which additionally indicates the median with its 90% confidence interval, the lower and upper quartile values, the most extreme values within 1.5 times of the interquartile range, and outliers of the measured distribution of parameters. The whole calculation took about 90 s per stack (20 z-images per stack/position) on a standard PC (Pentium D 2.80 GHz, 1 GB RAM). Apart from pre-processing steps and the statistical evaluation of the results, this included finding the sharpest image of each stack based on the local contrast estimation (∼20 s) and calculating the structure tensor components and from those the coherency measure (∼45 s).

Coherency as a Quantitative Measure for Structure

Cellular actin networks are organized in a complex manner over a hierarchy of different length scales. The exact structure of a given actin network is stochastic, because regulation by actin-binding proteins determines the molecular rules of network generation (like nucleation, branching, and capping of single filaments), but not its exact realization in space (36). In addition, the structure of actin networks depends on variable signals received from the environment, including the position of the cell adhesion contacts. Because of these stochastic effects, it is quite challenging to quantify specific structural changes. Finding a suitable parameter which is sensitive to the relevant changes in the network is a key issue, whereas different networks realized for the same set of rules should be ideally indistinguishable.

Because of the limited optical resolution of standard optical microscopes, like the ones used here, it is not possible to resolve the fine structure of the fibrous actin network in the cell. Thus, our analysis focused on prominent actin structures like stress fibers and the cortex at the cell boundaries, which lead to a typical spatial distribution of edges in the overall system. These considerations made us consider image coherency as a possible quantitative measure for alterations in the actin cytoskeleton. Coherency is defined through the structure tensor, which evaluates the local orientation in a small region of an image (26). A strategy to extract the local orientation $\hat{n}$ is

to assume that it deviates least from the gradient direction of the image gray values. This amounts to an extremum principle,

$$\int_{-\infty}^{\infty} w(\vec{x} - \vec{x}')(\hat{n} \cdot \nabla g(\vec{x}'))^2 \, d^2 x' \to \max, \qquad (1)$$

where $w(\vec{x} - \vec{x}')$ is a window function, constraining the neighborhood around pixel $\vec{x} = (x_1, x_2)$, and $\hat{n}$ is a unit vector defining the local orientation. In this consideration, the discrete gray values of the image are treated as a continuous scalar field $g(\vec{x})$. The optimization problem can be solved by rewriting Eq. (1) as

$$\hat{n}^T \mathbf{J} \hat{n} \to \max, \qquad (2)$$

where the structure tensor $\mathbf{J}$ is defined as,

$$J_{pq}(\vec{x}) = \int_{-\infty}^{\infty} w(\vec{x} - \vec{x}') \left(\frac{\partial g(\vec{x}')}{\partial x'_p} \frac{\partial g(\vec{x}')}{\partial x'_q} \right) d^2 x'. \qquad (3)$$

Using operator notation, the integral can be formulated as a convolution with a filter $\mathcal{G}$ which has the shape of the window function, whereas partial derivatives are approximated by discrete derivative operators $\mathcal{D}_{x_1}$ and $\mathcal{D}_{x_2}$, for which we chose the optimized Sobel filters (26),

$$J_{pq} \simeq \mathcal{G}\left(\mathcal{D}_{x_p} \cdot \mathcal{D}_{x_q} \right). \qquad (4)$$

Here, pixelwise multiplication is denoted by "·" to distinguish it from the successive application of convolution filters.

The structure tensor is symmetric; it is therefore reduced to a diagonal matrix by a suitable coordinate rotation. Hence, it is easy to show that the eigenvector to the largest eigenvalue λ_1 of the structure tensor maximizes Eq. (2) and defines the local orientation, whereas the magnitude of the squared gradient in this direction, averaged with respect to the window function, is related to the corresponding eigenvalue. To get a quality measure for the orientation, one can define the coherency by the squared relative difference of the two eigenvalues λ_1 and λ_2,

$$c_c = \left(\frac{\lambda_1 - \lambda_2}{\lambda_1 + \lambda_2} \right)^2 = \frac{(J_{22} - J_{11})^2 + 4J_{12}^2}{(J_{11} + J_{22})^2}. \qquad (5)$$

This parameter differentiates the two extreme cases: an area of constant gray values ($\lambda_1 = \lambda_2 = 0$) and an isotropic gray value structure ($\lambda_1 = \lambda_2 \neq 0$). Additionally, it serves as a measure for the difference of the dominant gradient compared to the gradient orthogonal to its direction (as the structure tensor is symmetric, its two eigenvectors are orthogonal and the eigenvalues are non-negative). Furthermore, it can be calculated right from the structure tensor components, Eq. (3), without the need to solve the eigenvalue problem. In general, the coherency varies continuously between 0, in regions without any dominant orientation, and 1, at perfectly oriented structures. Hence, it is also able to distinguish large-scale cytoskeleton constituents, like stress fibers or the cortex, from smaller actin speckles or the diffuse background in the cytosol and measures the amount and quality of structures in the cells on our images, accordingly. To overcome numerical instabilities when evaluating Eq. (5) at the singularity $\lambda_1 + \lambda_2 = 0$, we chose c_c to be zero for a small or vanishing denominator.

As the coherency is readily defined by the structure tensor in Eq. (3), the only free parameters in the calculations are determined by the shape and size of the window function, given by $\mathcal{G}$. We used a rotationally symmetric Gaussian smoothing operator of size $h_{\mathcal{G}}$ with standard deviation $\alpha_{\mathcal{G}}$. For good working conditions, the size and spread of the window function should be larger than the fine structure of edges to average out small-scale variations within the structures. However, finding the right size of the window function remains a trade off between averaging out noise and small artifacts, increasing its size, but sacrificing information about smaller structures.

Fig. 1 compares an original actin stain of a latrunculin B treated cell (a) with its coherency mapping as a function of the size of the window function (b–d). Apart from prominent cortical actin structures, small speckles are visible within the cell body, as a result of the treatment with the actin drug in the original image. The impact of such smaller structures is averaged out more and more in the feature images with increasing size of the window function. The large-scale structures, however, remain clearly visible and maintain a high coherency. On the basis of visual inspection of such images, we chose an intermediate size for the window function ($h_{\mathcal{G}} = 15$ and $\alpha_{\mathcal{G}} = 5$ pixel) to evaluate the images in section "Results".

Since we are using an automated image acquisition without any preselection for our experiments (cf. section "Automated microscopy and image processing"), the cell area as well as the number of cells in each image varies. To statistically evaluate and compare the results of several pictures with each other, some normalization procedure for the extracted parameters had to be introduced. On the one hand, we measured the total coherency of an image relative to the total cell area within the image and, on the other hand, the mean coherency. The coherency per cell area accounts for the amount or density of structures within the cells, whereas the mean coherency per image is a measure for the quality of the structures, independent of the frequency of their occurrence.

We segmented the cell area by applying Matlab's graythresh function to obtain a binary image and a subsequent hole filling procedure on the images. Concerning the experiments with adherent cells on HIV-1 coated substrates (section "HIV infected cells"), we used the actin stain for this routine, as it did not change in a way that altered the segmentation. However, for cells which were treated with actin drugs (section "Cells Treated with Actin Drugs"), we used an independent microtubule (MT) stain for the area estimation to rule out strong correlations between changes in the actin coherency/density and the cell area (Fig. 2). For all cytoskeleton model
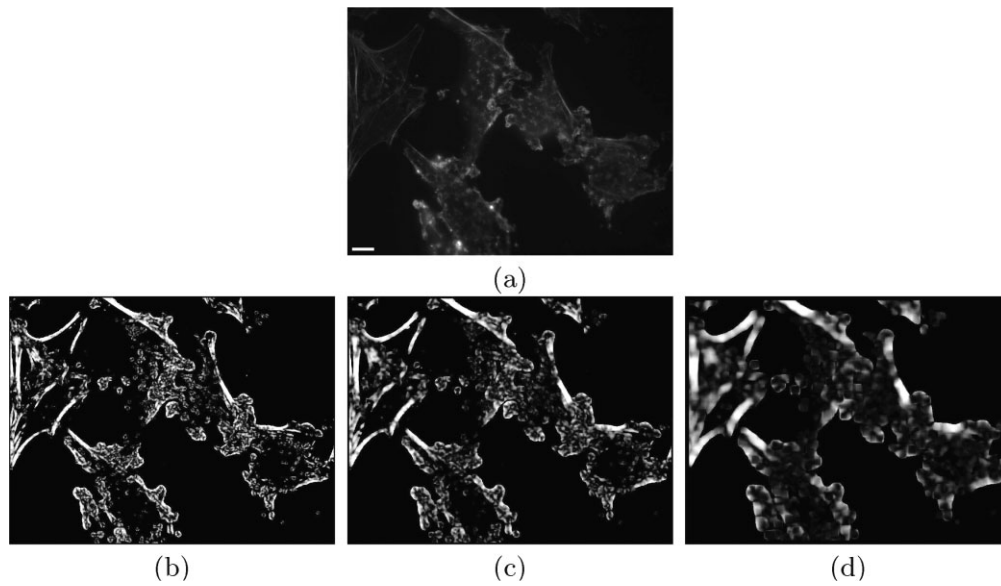
Figure 1. Impact of size and shape of the window function on the coherency image. (a) JC-53 cells treated with latrunculin B and stained for F-actin. In these cells, large-scale cortical structures are present, as well as small speckles due to the drug treatment. (Scale bar shows 10 μm) (b–d) Coherency images with $h_G = 9$, $\alpha_G = 3$ (b), $h_G = 15$ $\alpha_G = 5$ (c), and $h_G = 30$ $\alpha_G = 10$ (d). The size and spread are given in pixel. With increasing size of the window function, small structures are averaged out and lose weight in the coherency image.

images, the area was chosen to be constant (section "Analysis of the Model Cytoskeleton").

Biophysical Model for the Actin Cytoskeleton

Modeling the spatial organization of the actin cytoskeleton is a very active and increasingly sophisticated research field. To obtain a benchmark for our image processing setup, we used one of the simplest models, the Mikado model, or random fiber network (RFN), which has been used before to model the elasticity of the actin cytoskeleton (28). RFNs consist of an ensemble of randomly distributed and oriented straight rods in a two-dimensional environment. The network
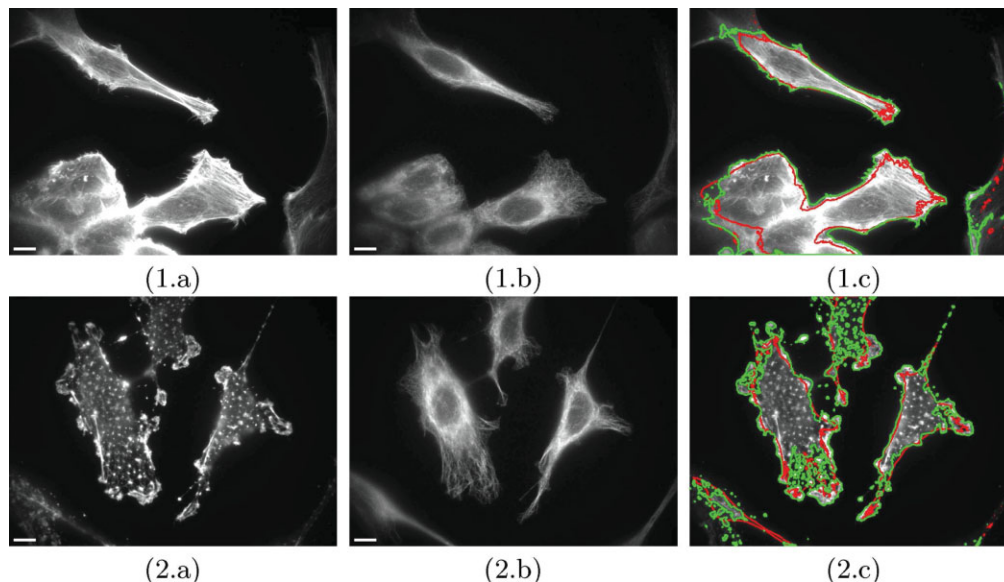

Figure 2. Effect of treatment with 1 μM latrunculin B. (1) Control cells; (2) inhibited cells; (a) actin stain; (b) MT stain; (c) segmented cell area for normalizing the extracted coherency and actin density according to Matlab's graythresh function using the actin (green) or MT (red) stain. The original actin stain is shown as well. For the control cells, the area segmentation according to both stains yields similar results, whereas, for the cells treated with latrunculin B, the size of the cell area is systematically under-estimated. To rule out correlations of the actin coherency and density with the segmented cell area, the segmentation was done according to an independent microtubule stain for the actin toxin experiments (section "Cells Treated with Actin Drugs"). Scale bars always represent 10 μm in the images. [Color figure can be viewed in the online issue, which is available at www.interscience.wiley.com.]

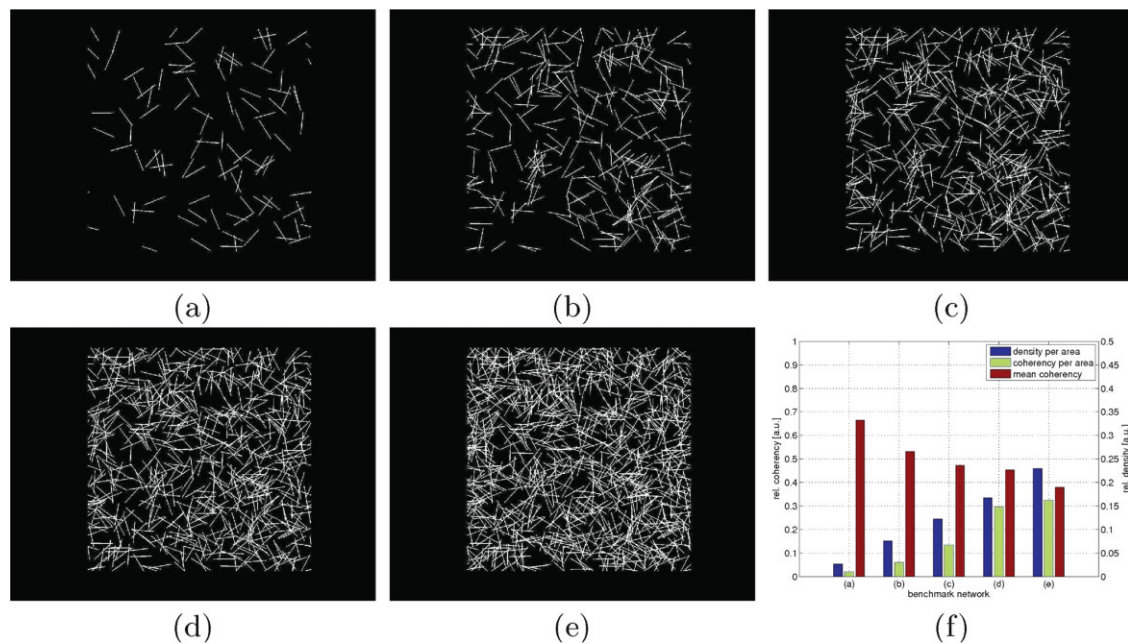**Figure 3.** Networks with an increasing total number of fibers. (a) $N_{fib} = 100$, (b) $N_{fib} = 300$, (c) $N_{fib} = 500$, (d) $N_{fib} = 700$, (e) $N_{fib} = 1,000$. (f) Plot of the extracted parameters, namely the averaged gray value density, the coherency per area, and the mean coherency of each image. [Color figure can be viewed in the online issue, which is available at www.interscience.wiley.com.]

holds a certain number N_{fib} of fibers, each of which is characterized by its position, orientation and length l_{fib}. In its original version, the model represents the ultrastructural F-actin network in the cell. However, as this length scale is beyond the resolution of our microscope, we had to adjust the model accordingly. For our purpose, each fiber in the network represents a bundle of actin filaments. Hence, we introduced two additional parameters in the model, namely the bundle strength s_{fib} and width w_{fib}, which parameterize the density and spatial extension of the bundle. We chose the position and orientation of each fiber uniformly randomly, whereas its length, number, width, and strength were either held constant or chosen from Gaussian random distributions, which are characterized by their mean and their standard deviation. Our simulated networks do not claim to reflect the detailed organization of single cells, but rather represent the average degree of network formation over an ensemble of many cells. Therefore, the simulated samples presented below (cf. Figs. 3–6) do not resemble the images of single cells, although the feature extraction does. Thus, it is possible to mimic versatile situations for structural changes in cells: the number of fibers, their length, strength, and width are increased individually to simulate the variable degree of structure formation in the cell. For a constant total fiber length in the images (which corresponds roughly to a stationary overall gray value density), the number of fibers is reduced. This mimics the depolymerization of actin bundles and the occurrence of small speckles induced by actin drugs.

RESULTS

Analysis of the Model Cytoskeleton

To evaluate the sensitivity of our image processing approach to changes within the actin cytoskeleton, we first applied it to our biophysical model. Computer-generated realizations of random fiber networks (RFNs) were used to elucidate the effect of changes in the modeling parameters (fiber number N_{fib}, length l_{fib}, strength s_{fib}, and width w_{fib}) on the feature parameters, which we extract from the images. We created five realizations of a single network as a function of one or two model parameters. As we initially analyzed only a single image as a representant for each realization, we first had to avoid strong stochastic variations in the networks. Therefore, all parameters, which were not changed explicitly, as well as the initial random positions and orientations of the fibers were kept constant throughout the different realizations. However, later we demonstrate the benefit of an automated technique, when dealing with large variations in the parameters over many realizations. In this case, the model parameters are not defined explicitly but rather the mean and the standard deviation of the corresponding Gaussian distributions. Subsequently, we applied our automated approach to a large number of images for each ensemble of networks.

We first tested the sensitivity of our image feature extraction to certain structural changes in the cytoskeleton. The nascence and growth of actin bundles due to cell adhesion was mimicked, increasing the fiber number, length, strength, and width individually. The disruption of stress fibers by depolymerizing actin drugs is simulated by an increasing fiber (or speckle) number for a constant total fiber length in the RFNs.

For an increasing number of fibers in the artificial networks (Figs. 3a–3e), the relative fiber density per area (blue), as well as the coherency per area (green), was increasing as expected (Fig. 3f). The mean coherency of the images (red) decreased with an increasing fiber number. As this parameter measures the average quality of structures independent of their
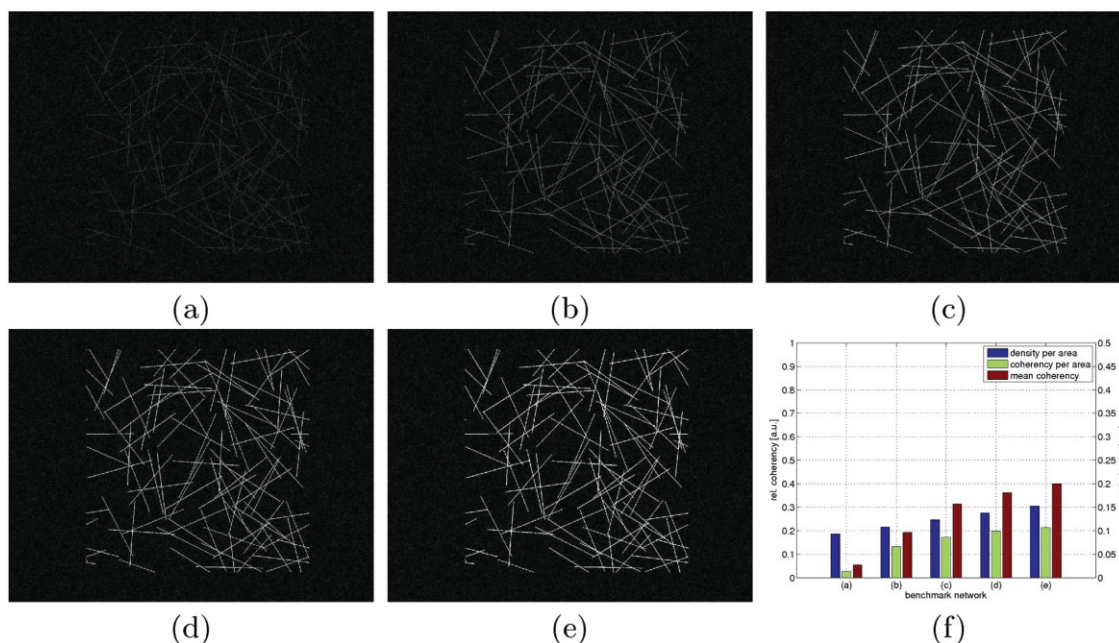
Figure 4. Networks with increasing fiber strength. (a) $s_{fib} = 0.2$, (b) $s_{fib} = 0.4$, (c) $s_{fib} = 0.6$, (d) $s_{fib} = 0.8$, (e) $s_{fib} = 1.0$. The fiber strength s_{fib} is defined as the intensity of the fiber gray values in the image in the range from 0 to 1. Gaussian white noise was added to the images. (f) Plot of the extracted image features. [Color figure can be viewed in the online issue, which is available at www.interscience.wiley.com.]

amount, it is in general possible that an image with only one fiber with perfectly oriented edges might have a higher mean coherency than an image with several fibers. In these examples, the quality was actually decreasing, because the crossing points between different fibers did not hold clear structural

details. As their number increased, the mean coherency decreased. Similar results were obtained for constant fiber number with an increasing length of each fiber (not shown).

For the simulated images, both coherency measures were not sensitive to an increase in fiber strength (i.e., mean gray
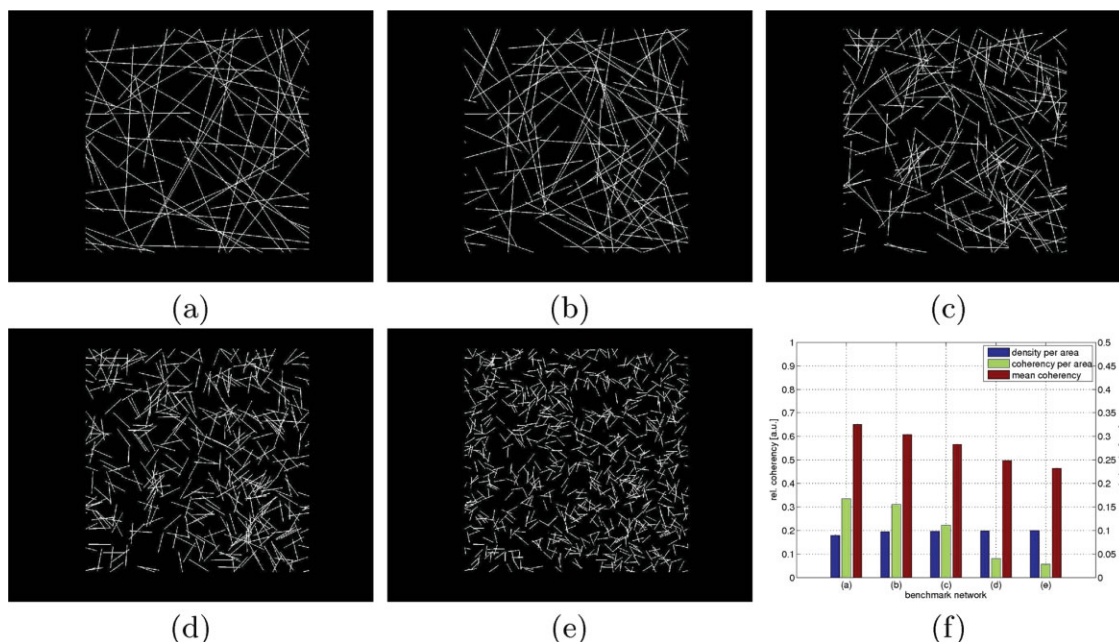

Figure 5. Networks with constant density. As the fiber length is reduced, their number is increased accordingly: (a) $N_{fib} = 50$, $l_{fib} = 8$, (b) $N_{fib} = 100$, $l_{fib} = 4$, (c) $N_{fib} = 200$, $l_{fib} = 2$, (d) $N_{fib} = 400$, $l_{fib} = 1$, (e) $N_{fib} = 800$, $l_{fib} = 0.5$; (The fiber length l_{fib} is defined relative to the network size 10 × 10.) This way, large-scale structures evolve, which can not be detected in the gray value density, but rather with either of the two relative coherency measures (f). [Color figure can be viewed in the online issue, which is available at www.interscience.wiley.com.]
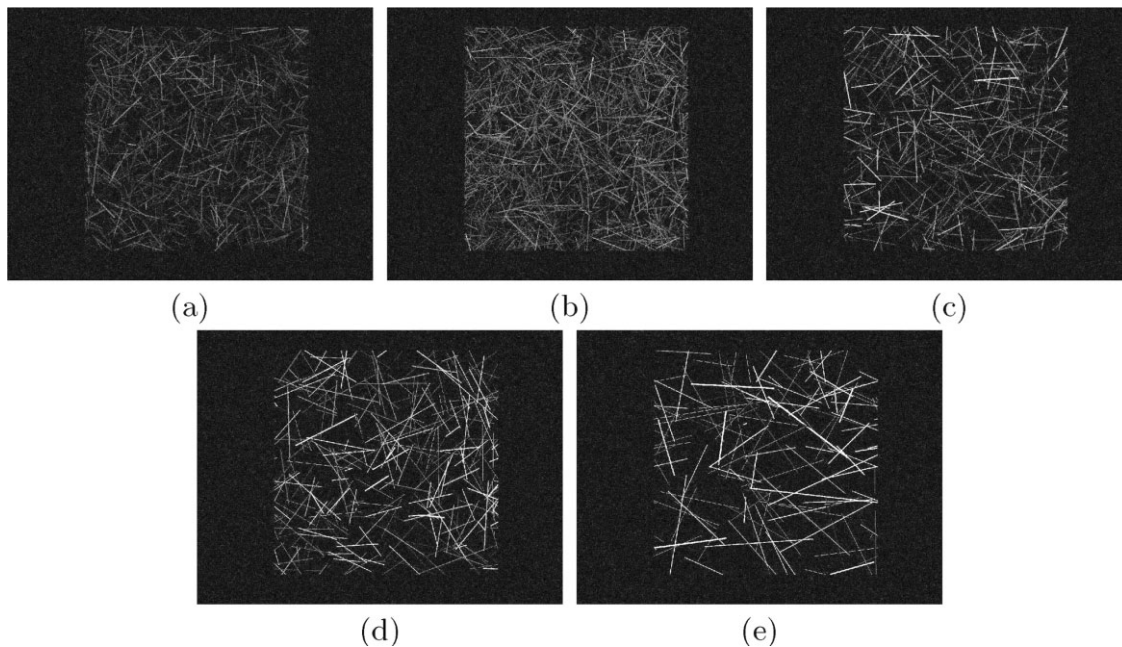
Figure 6. Examples for different network ensembles. The Gaussian parameter distributions of the fiber number, strength, and length have been chosen such that the mean gray value density remains roughly constant, but the quality and amount of the inherent structures increases: (a) $\langle N_{fib} \rangle = 2{,}250$, $\langle l_{fib} \rangle = 1$, $\langle s_{fib} \rangle = 0.2$, (b) $\langle N_{fib} \rangle = 1{,}500$, $\langle l_{fib} \rangle = 1.2$, $\langle s_{fib} \rangle = 0.25$, (c) $\langle N_{fib} \rangle = 750$, $\langle l_{fib} \rangle = 1.5$, $\langle s_{fib} \rangle = 0.4$, (d) $\langle N_{fib} \rangle = 375$, $\langle l_{fib} \rangle = 2$, $\langle s_{fib} \rangle = 0.6$, (e) $\langle N_{fib} \rangle = 150$, $\langle l_{fib} \rangle = 3$, $\langle s_{fib} \rangle = 1$; The standard deviation of the Gaussian distributions is always chosen relative to the corresponding mean at 0.5 $\langle X_{fib} \rangle$.

value of the fibers). This is due to the fact that the coherency does not measure the absolute gradient at the fiber edges, but rather compares the difference of the dominant squared gradient to its orthogonal counterpart, i.e., the two eigenvalues of the structure tensor. As we put perfect rods without any background noise in our benchmark images, there was basically just one non-vanishing gradient at the boundaries of the fibers, whereas the magnitude of the gradient orthogonal to the fiber edges was negligible. Therefore, the fiber strength itself was not detected by the coherency (not shown). However, the situation dramatically changed when we introduced additional Gaussian white noise to the same images, reflecting conditions of biological experiments (Fig. 4). In this case, the smaller eigenvalue of the structure tensor holds a finite value, and the absolute strength of the fibers indeed causes a difference in coherency. Both coherency measures are able to detect the difference in fiber strength much better than the relative fiber density.

In the previous examples, structural changes were not only detected by the coherency but also by the fiber density per area. In the following, however, the density of fibers was kept constant by increasing the fiber number, while reducing their length accordingly (Fig. 5). This procedure should simulate the disruption of stress fibers and occurrence of small speckles due to depolymerizing actin toxins. Here, both coherency measures were sensitive to the changes, but the relative actin density differed only slightly.
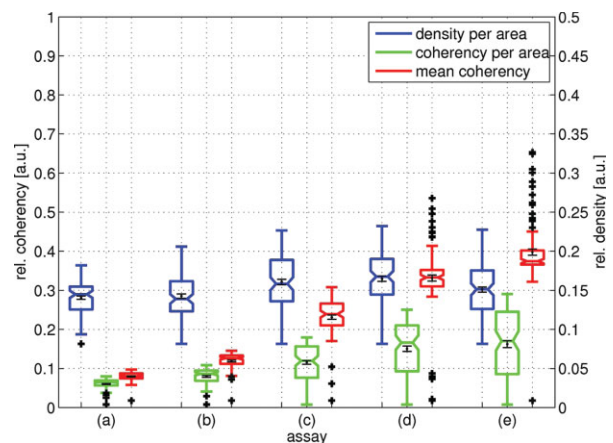

Figure 7. Box plots of the density per area (blue), coherency per area (green), and mean coherency (red), extracted from the network ensembles in Figures 6a–6e. For each parameter, the box plots indicate the estimated mean and its corresponding standard deviation (black dot with error bars), the median (horizontal line dividing the box), the lower and upper quartile, i.e., 25th and 75th percentile (lower and upper boundary of the box), the farthest measurement still within the 1.5 interquartile range (whiskers), outliers (+), and the symmetric 90% confidence intervals of the median (notches). Although the randomly chosen images in Figures 6a–6e cannot be clearly distinguished by eye, due to the strong variations in the parameters of the different ensembles, the statistical evaluation of the coherency from a large number of these images is able to average out non-specific variations, and is therefore sensitive to the changes in the network parameters. [Color figure can be viewed in the online issue, which is available at www.interscience.wiley.com.]
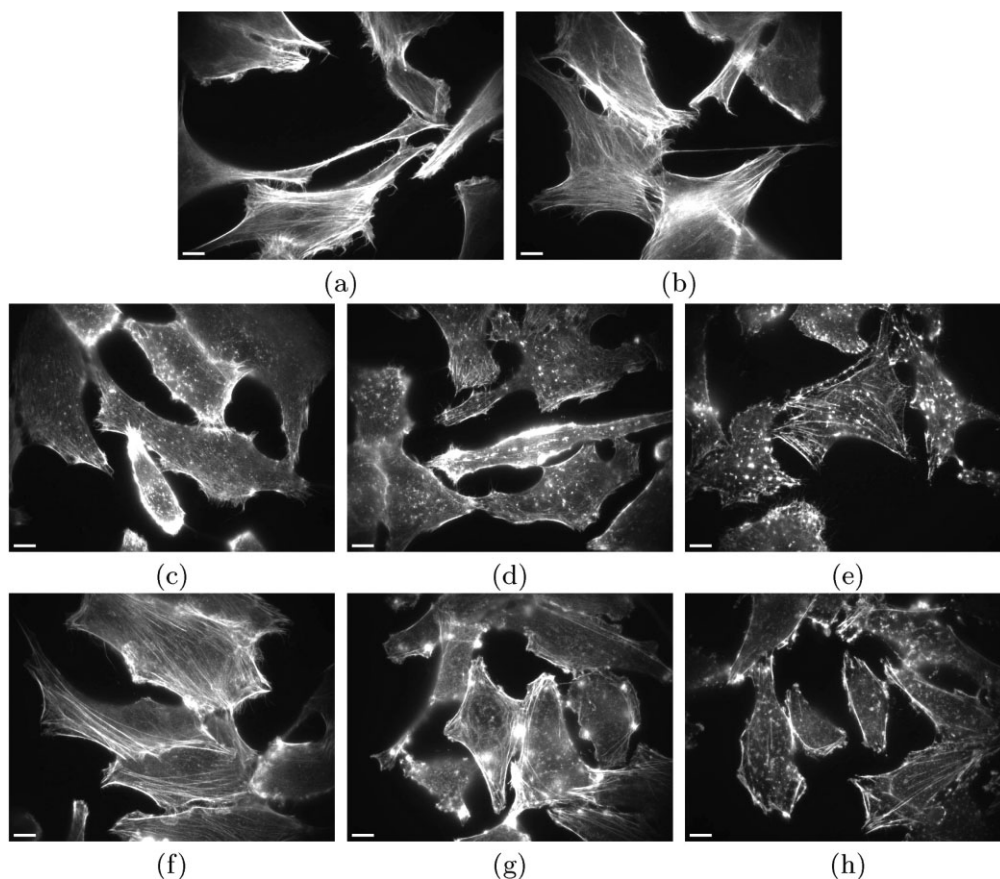
Figure 8. Randomly chosen images for the different assays: (a) control DMEM, (b) control DMSO, (c) cytochalasin D 0.5 μM, (d) cytochalasin D 1 μM, (e) cytochalasin D 2 μM, (f) latrunculin B 0.25 μM, (g) latrunculin B 0.5 μM, (h) latrunculin B 1 μM; each scale bar represents 10 μm.

Thus, in this case, extraction of coherency was required for correct analysis.

The benefit of computer-aided automatic image feature extraction clearly is the correct statistical evaluation of a large number of images, omitting the observer bias. Figures 6a–6e, feature randomly chosen representants of network ensembles, with respect to changing Gaussian distributions for the fiber number, strength, and width. Additionally, background noise was incorporated. These networks are highly variant, and it is now much harder to detect significant changes from the example images here by eye. The statistical evaluation of the coherency of a hundred images for each network type, however, was able to clearly detect the changes in the network structures (Fig. 7). As we averaged the parameters over several images for each network ensemble, an estimator for the standard deviation of the mean can be given accordingly, as well as a box plot of the measured parameter distribution. These networks were created with a roughly constant gray value density, and the density parameter was not able to detect a clear tendency in the changes. In contrast, both coherency measures revealed a clear tendency in the network differences from (a) to (e). These theoretical results justify to apply our newly developed procedure to experimental data.

Cells Treated with Actin Drugs

We next applied the automated image processing setup to cells treated with the actin toxins cytochalasin D and latrunculin B. Cytochalasin D leads to the depolymerization of F-actin, whereas latrunculin B inhibits actin polymerization by sequestering globular actin, resulting in the disruption of F-actin over time. We analyzed 96–100 images per assay in this experiment. Figure 8 shows an example for each experimental condition and Figure 9 displays the coherency results. Cells were either treated with increasing concentrations of one of the two actin toxins, or with solvent only.

Cytochalasin D treated cells exhibited a substantial decrease in either of the two coherency measures (c–e) compared to the controls (a and b), but no concentration-dependent differences. Measuring the actin density, in contrast, was unable to clearly differentiate the samples treated at the two lower concentrations of the toxin from the controls. For the lowest concentration of cytochalasin D, the relative actin density per cell area (c) was even larger than observed for the control populations. For latrunculin B (f–h), both parameters showed a clear decrease in coherency at higher toxin concentrations, whereas no difference was observed at the lower toxin concentration. No structural
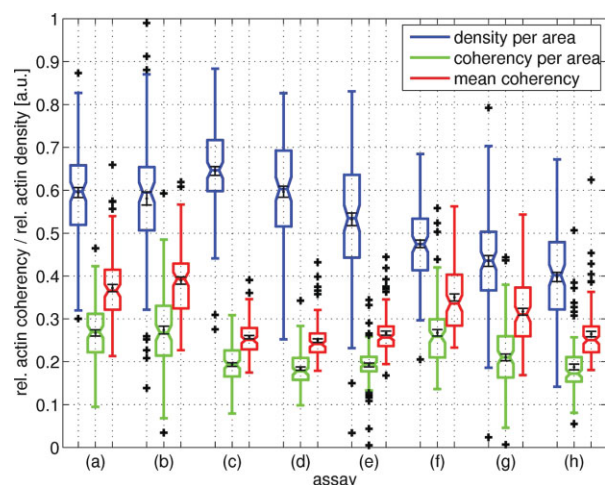
Quantifying the Actin Cytoskeleton

Figure 9. Box plots including the estimated mean and its standard deviation for the actin coherency and density of the cell ensembles shown in Figure 8. Control cells [(a) with DMEM and (b) with DMSO] are compared to cells treated with two concentrations of cytochalasin D [(c) 0.5 μM, (d) 1 μM, and (e) 2 μM] and latrunculin B [(f) 0.25 μM, (g) 0.5 μM, and (h) 1 μM]. The box plot setup is similar to Figure 7. [Color figure can be viewed in the online issue, which is available at www.interscience.wiley.com.]

Figure 10. Example for JC-53 cells on Lab-Teks which were precoated with HIV-1. Because of the experimental procedure, the plane of prominent actin structures (red) coincides with most HIV-1 particles (green). The scale is 10 μm. [Color figure can be viewed in the online issue, which is available at www.interscience.wiley.com.]

However, coherency is able to detect and quantify morphological differences induced by the actin toxins.

HIV-Infected Cells

We finally checked if HIV-1 binding to and entry into the cell, which is mediated by the viral envelope glycoprotein, detectably alters the actin cytoskeleton. To yield a maximum of virus-cell interactions in the focal plane at the bottom of the cell, JC-53 cells were seeded on 8-chambered Lab-Teks which were precoated with HIV-1 (cf. Fig. 10). To test whether possible effects are specific for HIV-1 and not simply due to the steric properties of the viral spheres, HIV-1 particles bearing or lacking the envelope glycoprotein were used.

Two independent experiments were performed, and the mean values of both coherency parameters as well as actin density were compared pairwise (cf. Figs. 11a and 11b). Apart from the usual variations, no difference in any of the three parameters was found over both experiments. We additionally performed similar statistical tests as before. They did not reveal a clear tendency for an HIV-1-specific effect on the structure of the actin cytoskeleton, concerning all three parameters for two independent experiments. Thus, interaction

differences were observed by visual inspection of cells treated with this toxin concentration, either. In all cases, a detailed analysis showed that the actin structures at the cell borders played a minor role for the coherency measure, which was dominated by the actin structures in the cell body due to its larger extension (data not shown).

We performed two-sided statistical tests of the null hypothesis which states that the means of two different assays in Figure 9 are equal, with a significance level of 5%. The corresponding P-values are given in Table 1. Under these circumstances, we accepted the hypothesis for the means of the two controls (a,b) in all three parameters. When we tested the hypothesis pairwise for actin toxin treated samples and the two controls, we could not reject the hypothesis for (a,d) and (b,d) in the density as well as (a,f) in both coherency measures, and (b,f) in the coherency per cell area, respectively. We conclude from this analysis, that actin density shows strong non-specific variations in the experiments and is therefore not a reliable measure for the structural changes of the actin cytoskeleton.

Table 1. P-values of the two sided statistical tests with the null hypothesis which states that the means of two different assays are equal

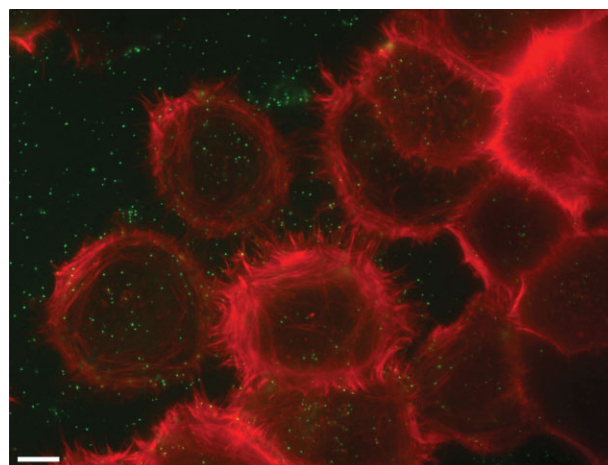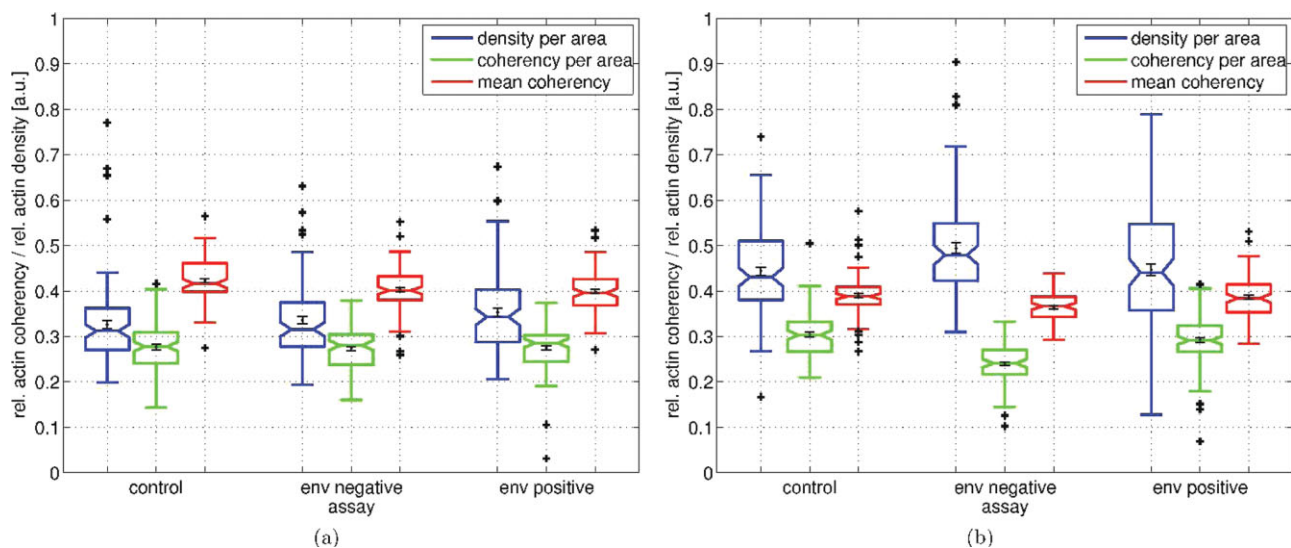|	(b)	(c)	(d)	(e)	(f)	(g)	(h)
Density per area (a)	0.236	0.0008	0.456	0.0005	$\leq 10^{-4}$	$\leq 10^{-4}$	$\leq 10^{-4}$
Density per area (b)		0.0003	0.214	0.01	$\leq 10^{-4}$	$\leq 10^{-4}$	$\leq 10^{-4}$
Coherency per area (a)	0.276	$\leq 10^{-4}$	$\leq 10^{-4}$	$\leq 10^{-4}$	0.486	$\leq 10^{-4}$	$\leq 10^{-4}$
Coherency per area (b)		$\leq 10^{-4}$	$\leq 10^{-4}$	$\leq 10^{-4}$	0.292	$\leq 10^{-4}$	$\leq 10^{-4}$
Mean coherency (a)	0.07	$\leq 10^{-4}$	$\leq 10^{-4}$	$\leq 10^{-4}$	0.33	$\leq 10^{-4}$	$\leq 10^{-4}$
Mean coherency (b)		$\leq 10^{-4}$	$\leq 10^{-4}$	$\leq 10^{-4}$	0.0005	$\leq 10^{-4}$	$\leq 10^{-4}$

Figure 11. Two experiments for the comparison of structures in cells on HIV-1 coated substrates compared to their control. (a) Cells were seeded for 120 min on a HIV-1 precoated substrate. (b) Same as (a) with seeding time of 70 min. [Color figure can be viewed in the online issue, which is available at www.interscience.wiley.com.]

of HIV-1 and the actin cytoskeleton might simply not result in detectable remodeling of the actin architecture. Yet another interpretation, fitting our experimental results, would be that remodeling rather occurs on the single particle level (e.g., only directly at the position of virus entry), and may only become evident at higher resolution. In these cases, our established microscopy workflow and image feature analysis would not be sensitive enough to deal with such subtle rearrangements of the actin structures.

CONCLUSION

We have shown that image coherency, i.e., the quality and amount of clear structures in an image, is a suitable measure to detect global alterations in the organization of the actin cytoskeleton. We could verify this theoretically, by artificially modeling a network with exactly defined properties, and experimentally, by measuring the impact of actin-disrupting drugs on coherency. We thereby established an automated workflow, combining high-content advanced fluorescence microscopy with a screening-like approach, subsequent computational image analysis and biophysical modeling. Because of our high-throughput approach, statistical failure was very low. We are therefore able to reliably detect even a very small effect on the actin coherency. Furthermore, an automated image acquisition and analysis excludes artifacts due to observer bias.

This procedure could be implemented for a wide range of biological applications dealing with structures accessible to microscopy. Here, we show that infecting susceptible cells with HIV-1 has no effect on the coherency of the actin cytoskeleton in the range of our resolution and detection limits, independent of virus amount and time. We cannot conclude that HIV-1 has no effect on the spatial organization of actin in its early lifecycle, but our results suggest that these effects — if any — are rather subtle. Either HIV-1-induced effects do not affect

actin coherency, or a potential impact on the coherency may only become evident at a higher resolution, and thus, needs super-resolution light or electron microscopy. Thus, even almost three decades after identification of HIV-1, exploring its interactions with the cytoskeleton remains a challenge.

Our study also shows that high-throughput microscopy not only requires automated image processing and statistical data analysis, but also can benefit from biophysical modeling. For the lamellipodium, the rapidly polymerizing actin network used by many cell types for propelling the cell forward, such an approach has already been adopted by different groups (17,37,38). Here, we introduce a similar approach for the actin cytoskeleton of stationary adherent cells. Without using the random fiber model, it would be difficult to appropriately benchmark the coherency measure. The underlying reason is that, although the actual structure of the cytoskeleton is determined by molecular rules guiding its assembly and disassembly in response to extracellular and intracellular signals, these rules determine the average structural features but not the exact details of each realization. As demonstrated here, one therefore has to use statistical modeling to assess the relevance of quantitative measures for spatial processes, like the structure of the actin cytoskeleton. We expect that, in the future, model-based analysis of high-throughput microscopy data becomes an important tool to study cellular structure on a systems level.

LITERATURE CITED

1. Howard J. Mechanics of motor proteins and the cytoskeleton. Sunderland, MA: Sinauer Associates; 2001.
2. Janmey PA. The cytoskeleton and cell signaling: Component localization and mechanical coupling. Physiol Rev 1998;78:763–781.

Quantifying the Actin Cytoskeleton

3. Mallik R, Gross SP. Molecular motors: Strategies to get along. Curr Biol 2004;14:971–982.

4. Jiménez-Baranda S, Gómez-Moutón C, Rojas A, Martínez-Prats L, Mira E, Lacalle RA, Valencia A, Dimitrov DS, Viola A, Delgado R, Carlos M-A, Santos M. Filamin-A regulates actin-dependent clustering of HIV receptors. Nat Cell Biol 2007;9:838–846.

5. Naghavi MH, Goff SP. Retroviral proteins that interact with the host cell cytoskeleton. Curr Opin Immunol 2007;19:402–407.

6. Wainberg MA, Jeang KT. 25 years of HIV-1 research: Progress and perspectives. BMC Med 2008;6:31.

7. Balabanian K, Harriague J, Decrion C, Lagane B, Shorte S, Baleux F, Virelizier JL, Arenzana-Seisdedos F, Chakrabarti LA. CXCR4-tropic HIV-1 envelope glycoprotein functions as a viral chemokine in unstimulated primary CD4+ T lymphocytes 1. J Immunol 2004;173:7150–7160.

8. Melar M, Ott DE, Hope TJ. Physiological levels of virion-associated human immunodeficiency virus type 1 envelope induce coreceptor-dependent calcium flux. J Virol 2007;81:1773–1785.

9. Lehmann MJ, Sherer NM, Marks CB, Pypaert M, Mothes W. Actin- and myosin-driven movement of viruses along filopodia precedes their entry into cells. J Cell Biol 2005;170:317–325.

10. Komano J, Miyauchi K, Matsuda Z, Yamamoto N. Inhibiting the Arp2/3 complex limits infection of both intracellular mature vaccinia virus and primate lentiviruses. Mol Biol Cell 2004;15:5197–5207.

11. Döhner K, Nagel CH, Sodeik B. Viral stop-and-go along microtubules: Taking a ride with dynein and kinesins. Trends Microbiol 2005;13:320–327.

12. Jolly C, Sattentau QJ. Retroviral spread by induction of virological synapses. Traffic 2004;5:643–650.

13. Fackler OT, Kräusslich HG. Interactions of human retroviruses with the host cell cytoskeleton. Curr Opin Microbiol 2006;9:409–415.

14. Bukrinskaya A, Brichacek B, Mann A, Stevenson M. Establishment of a functional human immunodeficiency virus type 1 (HIV-1) reverse transcription complex involves the cytoskeleton. J Exp Med 1998;188:2113–2125.

15. Lichtenstein N, Geiger B, Kam Z. Quantitative analysis of cytoskeletal organization by digital fluorescent microscopy. Cytometry A 2003;54A:8–18.

16. Verkhovsky AB, Chaga OY, Schaub S, Svitkina TM, Meister JJ, Borisy GG. Orientational order of the lamellipodial actin network as demonstrated in living motile cells. Mol Biol Cell 2003;14:4667–4675.

17. Fleischer F, Ananthakrishnan R, Eckel S, Schmidt H, Käs J, Svitkina T, Schmidt V, Beil M. Actin network architecture and elasticity in lamellipodia of melanoma cells. N J Phys 2007;9:420.

18. Echeverri CJ, Perrimon N. High-throughput RNAi screening in cultured cells: A user's guide. Nat Rev Genet 2006;7:373–384.

19. Paran Y, Lavelin I, Naffar-Abu-Amara S, Winograd-Katz S, Liron Y, Geiger B, Kam Z. Development and application of automatic high-resolution light microscopy for cell-based screens. Methods Enzymol 2006;414:228–247.

20. Perlman ZE, Slack MD, Feng Y, Mitchison TJ, Wu LF, Altschuler SJ. Multidimensional drug profiling by automated microscopy. Science 2004;306:1194–1198.

21. Matula P, Kumar A, Wörz I, Erfle H, Bartenschlager R, Eils R, Rohr K. Single-cell-based image analysis of high-throughput cell array screens for quantification of viral infection. Cytometry A 2009;75A:309–318.

22. Paran Y, Ilan M, Kashman Y, Goldstein S, Liron Y, Geiger B, Kam Z. High-throughput screening of cellular features using high-resolution light-microscopy: Application for profiling drug effects on cell adhesion. J Struct Biol 2007;158:233–243.

23. Boland MV, Murphy RF. A neural network classifier capable of recognizing the patterns of all major subcellular structures in fluorescence microscope images of HeLa cells. Bioinformatics 2001;17:1213–1223.

24. Conrad C, Erfle H, Warnat P, Daigle N, Lorch T, Ellenberg J, Pepperkok R, Eils R. Automatic identification of subcellular phenotypes on human cell arrays. Genome Res 2004;14:1130–1136.

25. Hamilton NA, Pantelic RS, Hanson K, Teasdale RD. Fast automated cell phenotype image classification. BMC Bioinformatics 2007;8:110–117.

26. Jähne B. Digital image processing. Berlin, Germany: Springer; 1997.

27. Raisch F, Scharr H, Kirchgeßner N, Jähne B, Fink RHA, Uttenweiler D. Velocity and feature estimation of actin filaments using active contours in noisy fluorescence image sequences. In: Proceedings of the International Conference on Visualization, Imaging and Image Processing, Malaga, Spain, September 9–12, 2002.

28. Wilhelm J, Frey E. Elasticity of stiff polymer networks. Phys Rev Lett 2003;91:108103.

29. Gallo RC, Sarin PS, Gelmann EP, Robert-Guroff M, Richardson E, Kalyanaraman VS, Mann D, Sidhu GD, Stahl RE, Zolla-Pazner S, Leibowitch J, Popovic M. Isolation of human T-cell leukemia virus in acquired immune deficiency syndrome (AIDS). Science 1983;220:865–867.

30. Platt EJ, Wehrly K, Kuhmann SE, Chesebro B, Kabat D. Effects of CCR5 and CD4 cell surface concentrations on infections by macrophagetropic isolates of human immunodeficiency virus type 1. J Virol 1998;72:2855–2864.

31. Matthews T, Salgo M, Greenberg M, Chung J, DeMasi R, Bolognesi D. Enfuvirtide: The first therapy to inhibit the entry of HIV-1 into host CD4 lymphocytes. Nat Rev Drug Discov 2004;3:215–225.

32. Coling D, Kachar B. Theory and application of fluorescence microscopy. Curr Protocols Neurosci, 2001;Chapter 2:Unit 2.1

33. Döhner K, Wolfstein A, Prank U, Echeverri C, Dujardin D, Vallee R, Sodeik B. Function of dynein and dynactin in herpes simplex virus capsid transport. Mol Biol Cell 2002;13:2795–2809.

34. Müller B, Daecke J, Fackler OT, Dittmar MT, Zentgraf H, Kräusslich HG. Construction and characterization of a fluorescently labeled infectious human immunodeficiency virus type 1 derivative. J Virol 2004;78:10803–10813.

35. Otsu N. A threshold selection method from gray-level histogram. IEEE Trans Syst, Man Cybern 1979;9:62–66.

36. Pollard TD, Berro J. Mathematical models and simulations of cellular processes based on actin filaments. J Biol Chem 2009;284:5433–5437.

37. Maly IV, Borisy GG. Self-organization of a propulsive actin network as an evolutionary process. Proc Nat Acad Sci USA 2001;98:11324–11329.

38. Ji L, Lim J, Danuser G. Fluctuations of intracellular forces during cell protrusion. Nat Cell Biol 2008;10:1393–1400.